

See discussions, stats, and author profiles for this publication at: <https://www.researchgate.net/publication/230764445>

# Oxygen reduction reaction activity of La-based perovskite oxides in alkaline medium: A thin-film rotating ring-disk electrode study

ARTICLE in THE JOURNAL OF PHYSICAL CHEMISTRY C · DECEMBER 2012

Impact Factor: 4.77 · DOI: 10.1021/jp211946n

---

CITATIONS

63

READS

368

---

## 5 AUTHORS, INCLUDING:



Jaka Sunarso

Curtin University

66 PUBLICATIONS 2,446 CITATIONS

[SEE PROFILE](#)



Wei Zhou

Nanjing Tech University

104 PUBLICATIONS 2,436 CITATIONS

[SEE PROFILE](#)



Patrick Howlett

Deakin University

76 PUBLICATIONS 2,721 CITATIONS

[SEE PROFILE](#)



Maria Forsyth

Deakin University

480 PUBLICATIONS 14,310 CITATIONS

[SEE PROFILE](#)

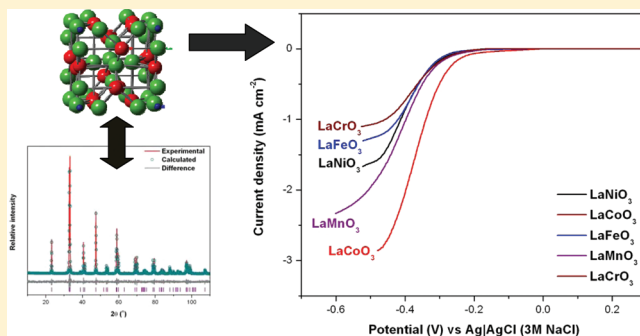
# Oxygen Reduction Reaction Activity of La-Based Perovskite Oxides in Alkaline Medium: A Thin-Film Rotating Ring-Disk Electrode Study

Jaka Sunarso,\*† Angel A. J. Torriero,† Wei Zhou,‡ Patrick C. Howlett,† and Maria Forsyth\*,†

†Australian Research Council (ARC) Centre of Excellence for Electromaterials Science, Institute for Technology Research and Innovation, Deakin University, 221 Burwood Hwy, Burwood, Victoria 3125, Australia

‡School of Chemical Engineering, The University of Queensland, Brisbane, Queensland 4072, Australia

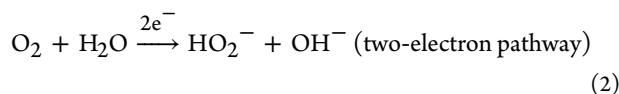
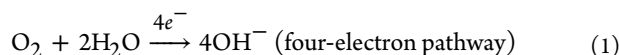
**ABSTRACT:** In this work,  $\text{LaMO}_3$  and  $\text{LaNi}_{0.5}\text{M}_{0.5}\text{O}_3$  ( $\text{M} = \text{Ni, Co, Fe, Mn and Cr}$ ) perovskite oxide electrocatalysts were synthesized by a combined ethylenediaminetetraacetic acid-citrate complexation technique and subsequent calcinations at 1000 °C in air. Their powder X-ray diffraction patterns demonstrate the formation of a specific crystalline structure for each composition. The catalytic property of these materials toward the oxygen reduction reaction (ORR) was studied in alkaline potassium hydroxide solution using the rotating disk and rotating ring-disk electrode techniques. Carbon is considered to be a crucial additive component because its addition into perovskite oxide leads to optimized ORR current density. For  $\text{LaMO}_3$  ( $\text{M} = \text{Ni, Co, Fe, Mn and Cr}$ ), in terms of the ORR current densities, the performance is enhanced in the order of  $\text{LaCrO}_3$ ,  $\text{LaFeO}_3$ ,  $\text{LaNiO}_3$ ,  $\text{LaMnO}_3$ , and  $\text{LaCoO}_3$ . For  $\text{LaNi}_{0.5}\text{M}_{0.5}\text{O}_3$ , the ORR current performance is enhanced in the order of  $\text{LaNi}_{0.5}\text{Fe}_{0.5}\text{O}_3$ ,  $\text{LaNi}_{0.5}\text{Co}_{0.5}\text{O}_3$ ,  $\text{LaNi}_{0.5}\text{Cr}_{0.5}\text{O}_3$ , and  $\text{LaNi}_{0.5}\text{Mn}_{0.5}\text{O}_3$ . Overall,  $\text{LaCoO}_3$  demonstrates the best performance. Most notably, substituting half of the nickel with cobalt, iron, manganese, or chromium translates the ORR to a more positive onset potential, suggesting the beneficial catalytic effect of two transition metal cations with Mn as the most promising candidate. Koutecky–Levich analysis on the ORR current densities of all compositions indicates that the four-electron pathway is favored on these oxides, which are consistent with hydroperoxide ion formation of <2%.



## INTRODUCTION

The air cathode in metal-air batteries, proton-exchange membrane fuel cells (PEMFCs), and anion-exchange membrane fuel cells (AMFCs) is one of the most expensive cell components and largely determines the cell performance.<sup>1</sup> This cathode catalyst is generally claimed to be responsible for at least 50% of the total cell cost.<sup>1</sup> This is due to the utilization of precious-metal-based catalysts such as Pt and Ag in the cathode because they have the highest oxygen reduction reactivity among all available electrocatalysts. To date, only a handful of non-metal-based catalysts show performance approaching those of Pt and Ag.<sup>2</sup> It is also widely known that the electrochemical kinetics of oxygen reduction at the cathode is substantially slower with respect to the anode and electrolyte electrochemical processes.<sup>3</sup> Therefore, numerous non-metal catalysts have been developed and screened in terms of their oxygen reduction reaction (ORR) activity.<sup>4–11</sup> In these studies, particularly, a thin-film, rotating ring-disk electrode (RRDE) technique is used whereby a very thin layer of electrocatalyst in a mixture with a conductive additive and binder (e.g., Nafion) is deposited onto a disk electrode.<sup>12</sup> This method eliminates the complication arising from mass transfer resistance of reactant (e.g., air) diffusion due to its absence in the thin-film and is much faster relative to the ORR measurement in fuel cells, which requires time-consuming optimization of membrane

electrode assemblies (MEAs).<sup>13</sup> Moreover, the ORR mechanisms in alkaline media, for example, whether ORR proceeds via two-electron (producing  $\text{HO}_2^-$ ) or four-electron (producing  $\text{H}_2\text{O}$ ) pathway (eqs 1 and 2),<sup>3</sup> can be simply monitored using a RRDE and applying a potential positive enough to the ring to oxidize the relative amount of  $\text{HO}_2^-$  formed in the disk-reduction process.<sup>14,15</sup>



Perovskite oxides with the  $\text{ABO}_3$  crystal structure formula are attractive as alternatives to noble metals because of their ORR activity and low cost.<sup>1,3</sup> In contrast with metal catalysts, which prefer acid environments for efficient ORR rates, perovskite oxides require an alkaline environment for favorable ORR activity to occur.<sup>2</sup> The perovskite crystal lattice is a host for a variety of mixed metal oxides (as represented by  $\text{A}_{1-x-y}\text{A}'_x\text{A}''_y\text{B}_{1-x-y}\text{B}'_x\text{B}''_y\text{O}_3$ ); the crystal structure and properties

Received: December 12, 2011

Revised: February 7, 2012

Published: February 9, 2012



(e.g., ionic transport properties and ORR activity) of which vary depending on the nature and relative amount of different elements in the A-site (lanthanides, e.g., La, Pr, and Gd or alkaline earth metals, e.g., Sr and Ba) and B-site cation (transition-metal elements, e.g., Mn, Co, Ni, Cr, and Fe).<sup>8,16</sup> In particular, the ORR activity of perovskites correlates strongly with the ability of B-site cation to adopt different valence states, which leads to the formation of redox couples at the potential of oxygen reduction.<sup>3</sup> Whereas a minor effect of different lanthanides in the constant valence A-site cation on the ORR activity has been studied with La demonstrating the best performance,<sup>17</sup> the effects of different transition metals and their combination on ORR activity is yet to be systematically investigated. This is despite a report that the presence of certain transition-metal elements in the B-site cation can have a significant impact on both ORR rates (e.g., with Mn, Co and Ni) and high chemical and electrochemical stability (e.g., Cr and Fe) in alkaline solution.<sup>1</sup>

To this end, the present Article is focused on La-based perovskite oxides, for example,  $\text{LaMO}_3$  and  $\text{LaNi}_{0.5}\text{M}_{0.5}\text{O}_3$ , where M = Ni, Co, Fe, Mn, and Cr. The interest in determining the effect of partially substituting Ni with another metal cation, as represented in the latter composition, arises from a recent report that claims  $\text{LaNiO}_3$  as one among the most promising compositions.<sup>8</sup> The structure and intrinsic ORR catalytic activity of the synthesized oxides are characterized and studied using powder X-ray diffraction (XRD) analysis and RRDE voltammetry, respectively. In addition, the ORR mechanism is thoroughly evaluated utilizing both Koutecky–Levich correlation and disk-ring current analysis.

## ■ EXPERIMENTAL SECTION

**Synthesis and Characterization.** Perovskite oxide powders were synthesized by a combined ethylenediaminetetraacetic acid (EDTA)-citrate complexing process. Rare-earth and transition-metal nitrates, for example,  $\text{La}(\text{NO}_3)_3 \cdot 6\text{H}_2\text{O}$  (99.99%, Sigma-Aldrich),  $\text{Ni}(\text{NO}_3)_2 \cdot 6\text{H}_2\text{O}$  (99.999%, Sigma-Aldrich),  $\text{Co}(\text{NO}_3)_2 \cdot 6\text{H}_2\text{O}$  (99.999%, Sigma-Aldrich),  $\text{Fe}(\text{NO}_3)_3 \cdot 9\text{H}_2\text{O}$  (99.99%, Sigma-Aldrich),  $\text{Mn}(\text{NO}_3)_2 \cdot 4\text{H}_2\text{O}$  (99.6%, Merck), and  $\text{Cr}(\text{NO}_3)_3 \cdot 9\text{H}_2\text{O}$  (99.0%, Sigma-Aldrich) were used as the metal ion precursors. Ethylenediaminetetraacetic acid ( $\text{C}_{10}\text{H}_{16}\text{N}_2\text{O}_8$ , 99.9%, Sigma-Aldrich) was first added under magnetic stirring to aqueous ammonium hydroxide ( $\text{NH}_3$ , 30%, Ajax Finechem). In a separate beaker, stoichiometric quantities of metal nitrates and citric acid ( $\text{C}_6\text{H}_8\text{O}_7$ , 99.5%, Sigma-Aldrich) were dissolved in deionized water. The EDTA solution was then added to the solution of metal nitrates and citric acid under stirring. The molar ratio of all metal nitrates/EDTA/citric acid normally needed to be kept at 1:1:2, whereas the final solution pH was controlled at 6 by adding ammonium hydroxide to ensure complete complexation was attained, as evidenced by the formation of colored transparent solution. Water evaporation was then performed slowly by heating to  $\sim 110^\circ\text{C}$ ; resulting in gel formation. The gel was then heated in a furnace at  $250^\circ\text{C}$  to form loose hardened gels, which can be easily recovered from the beaker and ground using mortar and pestle into powder. This powder was further calcined at  $1000^\circ\text{C}$  for 12 h in air to remove residual carbon and form final powder with well-crystallized structure. The resultant powder is milled (inside 50 mL yttria-stabilized zirconium jar utilizing 20 of 5 mm diameter alumina balls and ethanol as solvent) in planetary ball mill (Retsch PM 100) for 3 h to reach small and homogeneous particle size.

The crystal structures of the oxide powders were determined by XRD (Philips 1140/90) with filtered Cu  $\text{K}\alpha$  radiation at

40 kV and 25 mA, divergence slit of  $1^\circ$ , and a receiving slit of  $0.2^\circ$ . The diffraction patterns were collected at room temperature by step scanning in the range of  $10 \leq 2\theta \leq 90^\circ$ , with the scan rate of  $2^\circ \text{ min}^{-1}$ . Le Bail refinements on the XRD patterns were carried out using DIFFRACplus TOPAS 4.2 software.<sup>18</sup> All of the initial parameters for the structures were taken from PDF database.<sup>19</sup> During refinements, general parameters, such as the scale factor, background parameters, and the zero point of the counter, were optimized. Profile shape calculations were carried out using the Thompson–Cox–Hastings function implemented in the program by varying the strain parameter.

**Oxide Electrode Preparation.** The perovskite oxide powder (average particle of  $3 \mu\text{m}$  from scanning electron microscopy observation) was mixed with TIMCAL Super P Li carbon (average particle size of  $40 \text{ nm}^{20}$ ) at a 5:1 mass ratio of oxide to carbon to remove any electronic conductivity limitations within the thin film electrodes. The carbon was used as received. The catalyst suspension was prepared by sonication (Soniclean 160T, Soniclean Pty) of perovskite oxide and Super P Li carbon mixture with tetrahydrofuran (THF, 99.9+%, Sigma-Aldrich) for 1 h, resulting in ink with final concentrations of  $5 \text{ mg oxides mL}^{-1}$  and  $1 \text{ mg Super P Li mL}^{-1}$ . THF is chosen instead of acetone, ethanol, and water because the former solvent provided reasonably stable dispersion of oxide powder within the suspension whereas severe sedimentation could be instantly observed (even after only 1 min) on the suspensions utilizing the latter solvents. An aliquot of  $4 \mu\text{L}$  of suspension was drop-casted onto a glassy carbon disk electrode (4 mm diameter,  $0.126 \text{ cm}^2$  area, RRDE Pt Ring/GC disk electrode, ALS) previously polished with a  $0.05 \mu\text{m}$  alumina slurry (Buehler) on a clean polishing cloth (Buehler), sequentially rinsed with distilled water and acetone, and then dried with lint-free tissue paper. After slow evaporation of solvent,  $1 \mu\text{L}$  of Nafion solution (5 wt %, Fluka) was drop-casted on the electrode surface and dried slowly overnight inside a closed beaker to attach the catalyst particles onto the glassy carbon disk electrode. On the basis of the density of Nafion solution of  $\sim 0.874 \text{ g cm}^{-3}$  and density of Nafion film of  $\sim 2.0 \text{ g cm}^{-3}$ ,<sup>12</sup> an estimated Nafion film thickness of  $\sim 1.74 \mu\text{m}$  is obtained, which is reasonably thin to render a negligible  $\text{O}_2$  transport resistance within the film.<sup>21</sup>

**Electrochemical Characterization.** Voltammetric experiments were performed with a Biologic VMP2/Z multichannel potentiostat. RRDE voltammograms were obtained in a 0.1 M potassium hydroxide (KOH) prepared from deionized water and KOH pellets (99.99%, Sigma-Aldrich) at  $20 \text{ mV s}^{-1}$  in either  $\text{N}_2$  or  $\text{O}_2$  (ultrahigh purity grade, BOC) at room temperature (which corresponds to electrolyte temperature of  $\sim 17 \pm 1^\circ\text{C}$ ). Voltammograms for the reduction of oxygen and simultaneous oxidation of  $\text{HO}_2^-$  were obtained using a four-electrode arrangement in a 100 mL glass cell vial utilizing RRDE-3A rotating ring/disk electrode apparatus (ALS, Japan). This consists of a glassy carbon disk electrode ( $0.126 \text{ cm}^2$  area), a Pt ring electrode ( $0.189 \text{ cm}^2$  area, ALS, Japan), a platinum wire counter electrode, and a  $\text{Ag}/\text{AgCl}$  (3 M NaCl) reference electrode (RE-1B, ALS, Japan). The ring potential was set at 0.47 V versus  $\text{Ag}/\text{AgCl}$  (3 M NaCl), which is considered to be sufficiently high to induce complete  $\text{HO}_2^-$  decomposition as reported elsewhere.<sup>14,15</sup> For this experiment, two synchronized potentiostat channels were used simultaneously to enable disk-ring electrode potential–current measurements. Rotating disk electrode experiments were obtained using a conventional three-electrode arrangement consisting of a 3 mm diameter Pt disk electrode ( $0.071 \text{ cm}^2$  area, ALS, Japan) and

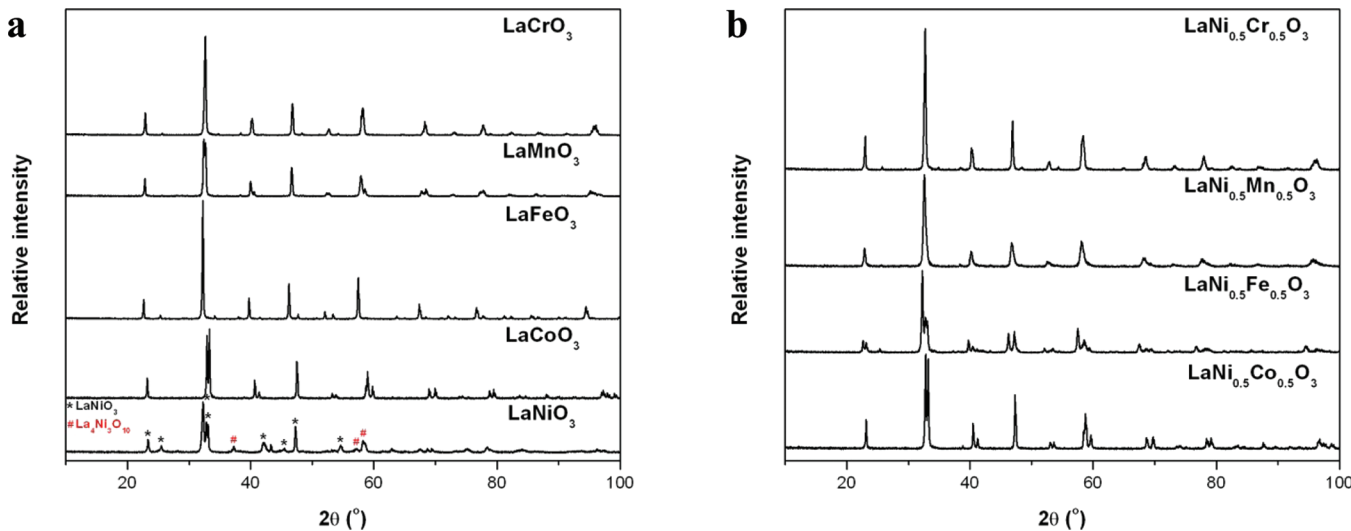


**Figure 1.** X-ray diffraction (XRD) patterns of (a)  $\text{LaNiO}_3$ ,  $\text{LaCoO}_3$ ,  $\text{LaFeO}_3$ ,  $\text{LaMnO}_3$ , and  $\text{LaCrO}_3$  and (b)  $\text{LaNi}_{0.5}\text{Co}_{0.5}\text{O}_3$ ,  $\text{LaNi}_{0.5}\text{Fe}_{0.5}\text{O}_3$ ,  $\text{LaNi}_{0.5}\text{Mn}_{0.5}\text{O}_3$ , and  $\text{LaNi}_{0.5}\text{Cr}_{0.5}\text{O}_3$ .

**Table 1. Phase Identification and Le Bail Refinement Summary from X-ray Diffraction Patterns<sup>a</sup>**

composition	$\text{LaNiO}_3$	$\text{LaCoO}_3$	$\text{LaFeO}_3$	$\text{LaMnO}_3$	$\text{LaCrO}_3$
phase	first	second	all	all	all
compound (closest match)	$\text{LaNiO}_3$	$\text{La}_4\text{Ni}_3\text{O}_{10}$	$\text{LaCoO}_3$	$\text{LaFeO}_3$	$\text{La}_{1-x}\text{Mn}_{1-z}\text{O}_3$
JCPDS-ICDD PDF no.	00-012-0751	00-035-1242	<b>00-048-0123</b>	<b>00-037-1493</b>	<b>00-051-1514</b>
crystal structure		orthorhombic	trigonal	orthorhombic	orthorhombic
space group (no.)			$\bar{R}\bar{3}c$ (167)	$Pnma$ (62a)	$R\bar{3}m$ (160)
<i>a</i> (Å)			5.44535(13)	5.56638(26)	5.52719(31)
<i>b</i> (Å)				7.85923(44)	5.51777(33)
<i>c</i> (Å)			13.09700(34)	5.55713(32)	6.68074(48)
$\chi^2$			1.05	1.28	1.21
$R_p$			0.1485	0.1984	0.1967
$R_{wp}$			0.2033	0.3273	0.2962
$R_{exp}$			0.1941	0.2565	0.2453
$R_{bragg}$			0.0101	0.9989	0.0255

<sup>a</sup>JCPDS-ICDD PDF no. in italics provides the initial structure and parameters for Le Bail refinements.

similar counter and reference electrodes used in RRDE experiments. The background capacitive current contribution (obtained from nitrogen-saturated experiment) is subtracted from each voltammogram. Three perovskite films were prepared for each composition to check the reproducibility of the film quality and performance; the results of which vary within the experimental error.

## RESULTS AND DISCUSSION

**Powder X-ray Diffraction Characterization.** Powder XRD patterns of the synthesized perovskite oxides (Figure 1a,b) show the formation of crystalline structures evidenced by the presence of regular group of peaks at different angles, which arises from particular set of reflections. Detailed analysis for each composition using a peak matching procedure to the powder XRD database<sup>19</sup> is listed in Tables 1 and 2, where the closest matching in terms of the structure and space group is displayed. Le Bail refinement fittings are then used to confirm the structure and obtain the lattice parameter values on those compositions, where their initial lattice parameter values can be found from database. The typical Le Bail refinement result is shown in Figure 2 for  $\text{LaCoO}_3$ , which indicates that reasonably good fitting is attained. The reliability factors of the refinements are also included in Tables 1 and 2. These Tables denote that the synthesized  $\text{LaCoO}_3$  and  $\text{LaNi}_{0.5}\text{Co}_{0.5}\text{O}_3$  as well as  $\text{LaNi}_{0.5}\text{Mn}_{0.5}\text{O}_3$  and  $\text{LaNi}_{0.5}\text{Cr}_{0.5}\text{O}_3$

have similar specific structures, for example, trigonal with space group  $\bar{R}\bar{3}c$  and cubic with space group  $Pm\bar{3}m$ , respectively.  $\text{LaNiO}_3$ , particularly, contains two different phases (refer to Figure 1a), one of which matches the set of peaks belonging to  $\text{LaNiO}_3$  reported in powder diffraction file (PDF) no. 00-012-0751, and another set of peaks belongs to orthorhombic  $\text{La}_4\text{Ni}_3\text{O}_{10}$ , as reported in PDF no. 00-035-1242.<sup>19</sup> Notably, the lattice structure of the first phase is not provided in the PDF, and the use of an indexing procedure in DIFFRACplus TOPAS 4.2<sup>18</sup> does not lead to a confident result. All other compositions demonstrate that the formation of distinct structure belongs to either trigonal or orthorhombic lattices.

**Electrochemical Characterization.** Figure 3a shows cyclic voltammograms representing the ORR in 0.1 M KOH using a thin film of  $\text{LaNiO}_3$ , carbon, and  $\text{LaNiO}_3$ –carbon mixture deposited on the rotating disk working electrode, which was rotated at 1600 rpm during the experiment. As a control experiment, a nitrogen ( $\text{N}_2$ )-saturated solution displays no noticeable reduction feature between  $-0.6$  and 0 V, which is to be expected due to the absence of oxygen. The use of a glassy carbon disk electrode (the substrate onto which the film is deposited) in an oxygen ( $\text{O}_2$ )-saturated system leads to an onset of reduction current at approximately  $-0.15$  V, which increases gradually in the potential window studied (up to  $-0.6$  V).

**Table 2.** Phase Identification and Le Bail Refinement Summary from X-ray Diffraction Patterns (Continuing Table 1)<sup>a</sup>

composition	LaNi <sub>0.5</sub> Co <sub>0.5</sub> O <sub>3</sub>	LaNi <sub>0.5</sub> Fe <sub>0.5</sub> O <sub>3</sub>	LaNi <sub>0.5</sub> Mn <sub>0.5</sub> O <sub>3</sub>	LaNi <sub>0.5</sub> Cr <sub>0.5</sub> O <sub>3</sub>
phase	all	all	all	all
compound (closest match)	LaNi <sub>0.6</sub> Co <sub>0.4</sub> O <sub>3</sub>	LaNi <sub>0.9</sub> Fe <sub>0.1</sub> O <sub>3</sub>	LaMnO <sub>3</sub>	LaCrO <sub>3</sub>
JCPDS-ICDD PDF no.	<b>00-032-0296</b>	01-088-0634	<b>01-075-0440</b>	<b>01-075-0441</b>
crystal structure	trigonal	trigonal	cubic	cubic
space group (no.)	R <bar{3}c (167)<="" td=""><td></td><td>Pm<bar{3}m (221)<="" td=""><td>Pm<bar{3}m (221)<="" td=""></bar{3}m></td></bar{3}m></td></bar{3}c>		Pm <bar{3}m (221)<="" td=""><td>Pm<bar{3}m (221)<="" td=""></bar{3}m></td></bar{3}m>	Pm <bar{3}m (221)<="" td=""></bar{3}m>
<i>a</i> (Å)	5.46647(19)		3.88135(77)	3.88064(21)
<i>b</i> (Å)				
<i>c</i> (Å)	13.13605(52)			
$\chi^2$	1.07		1.33	1.36
<i>R</i> <sub>p</sub>	0.1504		0.2120	0.2056
<i>R</i> <sub>wp</sub>	0.2112		0.2934	0.3012
<i>R</i> <sub>exp</sub>	0.1980		0.2205	0.2215
<i>R</i> <sub>bragg</sub>	0.0133		0.0316	0.0263

<sup>a</sup>JCPDS-ICDD PDF no. in italic provides the initial structure and parameters for Le Bail refinements.

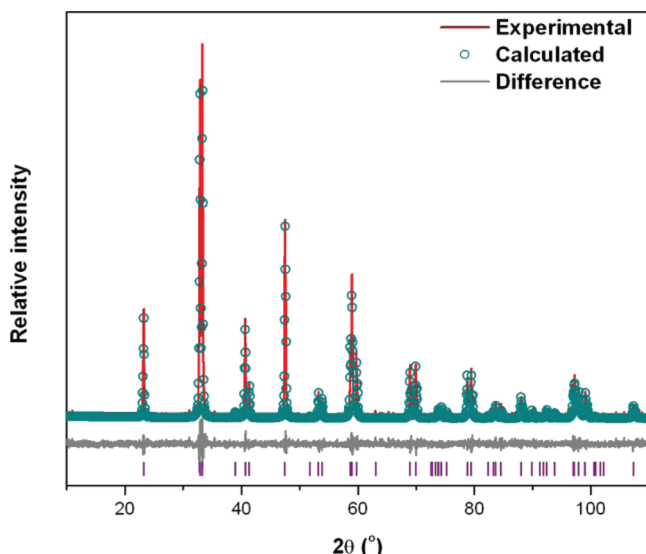


**Figure 2.** Typical Le Bail refinement fitting for XRD patterns shown in Figure 1 (represented here by LaCoO<sub>3</sub>).

The observed current, nevertheless, is negligible with respect to the reduction currents observed when a LaNiO<sub>3</sub>, carbon, and

LaNiO<sub>3</sub>–carbon film is deposited on top of glassy carbon electrode, indicating that the three latter modified electrodes contribute catalytic effects toward enhanced ORR. In particular, the ORR current is improved in the order of LaNiO<sub>3</sub>, carbon, and LaNiO<sub>3</sub>–carbon. Evidently, using LaNiO<sub>3</sub> without carbon brings about a worse performance relative to carbon; this is most likely associated with nonhomogeneous electron transfer inside the film due to poor electronic conductivity. Adding carbon to LaNiO<sub>3</sub>, in turn, leads to enhancement over the sole carbon performance, suggesting a synergistic effect of their combination. This is in good agreement with a previous report on La<sub>0.6</sub>Ca<sub>0.4</sub>CoO<sub>3</sub>–carbon thin film electrode, where Li et al. attributed this effect to the relatively faster electron-transfer reaction facilitated by cooperation between the oxide and carbon (relative to each by itself); for example, O<sub>2</sub> is first reduced in alkaline media through two electron pathway to HO<sub>2</sub><sup>-</sup> at more active carbon sites, followed by HO<sub>2</sub><sup>-</sup> reduction to OH<sup>-</sup> at adjacent oxide sites.<sup>15</sup> Therefore, in all subsequent experiments, carbon is added in the thin perovskite oxides film electrodes. To simplify the notation, all subsequent figures would only display the oxide composition (whereas in actual this refers to oxide and carbon mixture). Figure 3b shows the typical ORR current densities as a function of rotation rate from 200 to 1600 rpm. For LaNiO<sub>3</sub>, the ORR operates under mixed kinetic-diffusion-controlled regime in the potential range of −0.2 to approximately

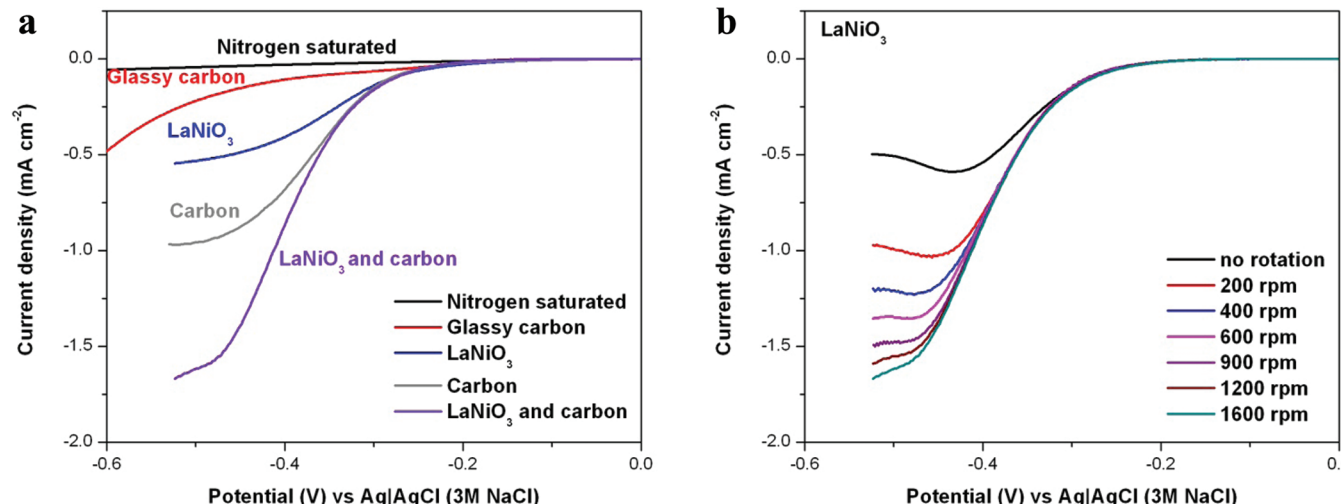


**Figure 3.** (a) Background (nitrogen saturated) and oxygen reduction reaction (ORR) current densities at 1600 rpm. (b) ORR currents of LaNiO<sub>3</sub> at different rotation rates (up to 1600 rpm) (all in oxygen saturated 0.1 M KOH electrolyte using negative scan direction at 20 mV s<sup>-1</sup> scan rate).

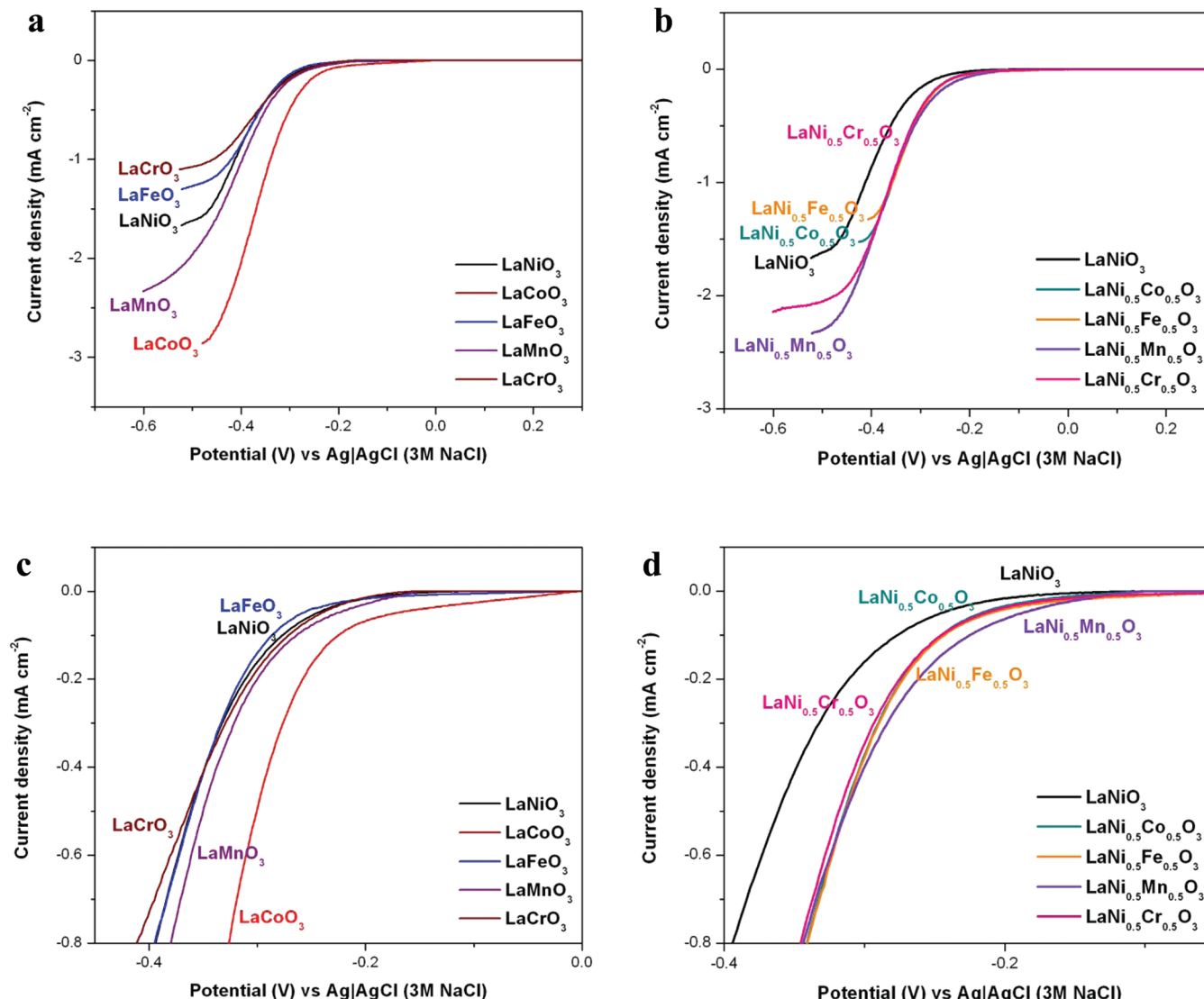


**Figure 4.** ORR current densities of thin film of (a) LaNiO<sub>3</sub>, LaCoO<sub>3</sub>, LaFeO<sub>3</sub>, LaMnO<sub>3</sub>, and LaCrO<sub>3</sub> and (b) LaNi<sub>0.5</sub>Co<sub>0.5</sub>O<sub>3</sub>, LaNi<sub>0.5</sub>Fe<sub>0.5</sub>O<sub>3</sub>, LaNi<sub>0.5</sub>Mn<sub>0.5</sub>O<sub>3</sub>, and LaNi<sub>0.5</sub>Cr<sub>0.5</sub>O<sub>3</sub> (all in oxygen-saturated 0.1 M KOH electrolyte using negative scan direction at 20 mV s<sup>-1</sup> scan rate). (c,d) Magnified portion to pinpoint the onset ORR potentials on panels a and b, respectively.

–0.47 V. At potential values more negative than approximately –0.47 V, current plateau seems to prevail; indicating the domination of diffusion-limiting regime. Closer observation of the shape of the diffusion-limited ORR current section in Figure 3b reveals its gradual change from transient-like behavior to a steady-state curve upon increasing the rotation rate from 200 to 1600 rpm. Li et al. observed similar features, which they explained was related to the presence of adsorbed O<sub>2</sub> inside the electrode film.<sup>15</sup> Accordingly, at lower rotation rates, a larger amount of O<sub>2</sub> is adsorbed in the film, leading to the more noticeable occurrence of an electroreduction current (represented by the peak) prior to the electroreduction current of O<sub>2</sub> in the bulk electrolyte.

Voltammograms obtained for the ORR in oxygen-saturated 0.1 M KOH for all synthesized perovskite oxides at 1600 rpm rotation rate are depicted in Figure 4a,b. For comparison, and to clearly display the onset potential, a portion of these graphs is magnified and is presented in Figure 4c,d. Figure 4a reveals that among LaNiO<sub>3</sub>, LaCoO<sub>3</sub>, LaFeO<sub>3</sub>, LaMnO<sub>3</sub>, and LaCrO<sub>3</sub>, LaCoO<sub>3</sub> demonstrates the largest diffusion-limited ORR current density, followed by LaMnO<sub>3</sub>, LaNiO<sub>3</sub>, LaFeO<sub>3</sub>, and

LaCrO<sub>3</sub> in decreasing order. This trend is almost similar with respect to the onset potentials (Figure 4c), for example, the composition, which has the larger current density, also displays a more positive ORR onset potential. The only noticeable exceptions to this are LaFeO<sub>3</sub> and LaCrO<sub>3</sub>, the latter of which starts ORR at a more positive potential yet shows lower diffusion limited ORR current with respect to the former one. Partially substituting half of the nickel with other metals, for example, Co, Fe, Mn, and Cr, causes the onset potential to occur at more positive potentials (Figure 4c,d), suggesting the beneficial catalytic effect from two transition metals presence. This observation partially supports the thinking that the ORR activity of perovskite is indeed strongly correlated with the valence state of transition-metal cation including its change during reduction–oxidation reaction. The diffusion-limited ORR current density magnitude in Figure 4b decreases in the order of LaNi<sub>0.5</sub>Mn<sub>0.5</sub>O<sub>3</sub>, LaNi<sub>0.5</sub>Cr<sub>0.5</sub>O<sub>3</sub>, LaNiO<sub>3</sub>, LaNi<sub>0.5</sub>Co<sub>0.5</sub>O<sub>3</sub>, and LaNi<sub>0.5</sub>Fe<sub>0.5</sub>O<sub>3</sub>. In terms of onset potential, LaNi<sub>0.5</sub>Mn<sub>0.5</sub>O<sub>3</sub> and LaNiO<sub>3</sub> provide the best and worst performance, respectively (assuming onset at more positive potential equals to better

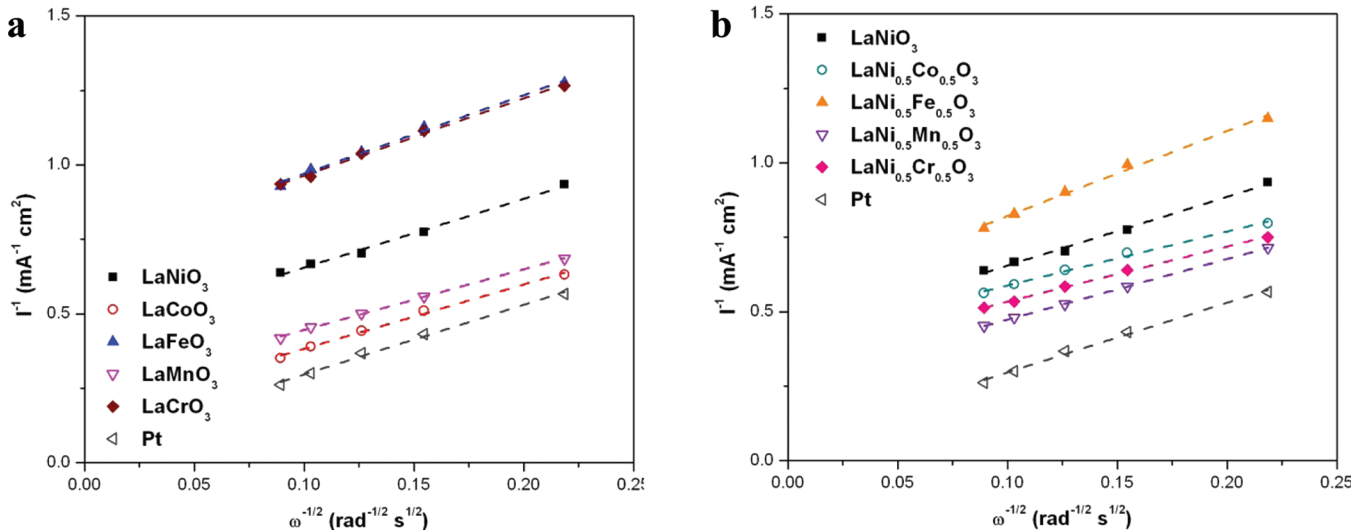


**Figure 5.** Koutecky–Levich plots for ORR current densities of thin film of (a)  $\text{LaNiO}_3$ ,  $\text{LaCoO}_3$ ,  $\text{LaFeO}_3$ ,  $\text{LaMnO}_3$ , and  $\text{LaCrO}_3$  and (b)  $\text{LaNi}_{0.5}\text{Co}_{0.5}\text{O}_3$ ,  $\text{LaNi}_{0.5}\text{Fe}_{0.5}\text{O}_3$ ,  $\text{LaNi}_{0.5}\text{Mn}_{0.5}\text{O}_3$ , and  $\text{LaNi}_{0.5}\text{Cr}_{0.5}\text{O}_3$ .

catalytic activity). Unfortunately, the differences in the onset potential for  $\text{LaNi}_{0.5}\text{Cr}_{0.5}\text{O}_3$ ,  $\text{LaNi}_{0.5}\text{Co}_{0.5}\text{O}_3$ , and  $\text{LaNi}_{0.5}\text{Fe}_{0.5}\text{O}_3$  cannot be clearly determined because of their substantially overlapping current profiles (Figure 4d).

The ORR mechanism was further examined using the Koutecky–Levich correlations, which are plotted in Figure 5a,b. For Nafion-coated oxide electrodes, these correlations are represented by the following equations

$$\frac{1}{i_d} = \frac{1}{i_k} + \frac{1}{i_f} + \frac{1}{i_{dl}} \quad (3)$$

$$i_k = nFAkC_{\text{O}_2} \quad (4)$$

$$i_{dl} = 0.20nFAC_{\text{O}_2}D_{\text{O}_2}^{2/3}\nu^{-1/6}\omega^{1/2} = Bn\omega^{1/2} \quad (5)$$

$$i_f = nFAC_{\text{O}_2}^f D_{\text{O}_2}^f L^{-1} \quad (6)$$

where  $i_d$ ,  $i_k$ ,  $i_{dl}$ , and  $i_f$  are the disk current density, kinetic current density, diffusion-limiting current density, and film diffusion-limiting current density, respectively. Furthermore,  $n$  is the number of electrons in the ORR,  $F$  is the Faraday constant ( $96\ 500\ \text{C mol}^{-1}$ ),  $A$  is the area of the disk electrode ( $0.126\ \text{cm}^2$ ),  $C_{\text{O}_2}$  is the oxygen concentration in the electrolyte,  $D_{\text{O}_2}$  is the oxygen diffusion coefficient ( $\text{cm}^2\ \text{s}^{-1}$ ),  $\nu$  is the kinematic viscosity of the electrolyte ( $\text{cm}^2\ \text{s}^{-1}$ ),  $\omega$  is the electrode rotation rate (rpm),  $k$  is the rate constant for the ORR, and  $L$  is the film thickness.

All plots in Figure 5a,b demonstrate linear and parallel features, implying a first-order dependence of  $\text{O}_2$  kinetics on all perovskite oxides.<sup>14,15,22</sup> Moreover, the slope of all plots is related to the number of electrons involved in the ORR according to eq 5 (noting that slope of plot equals to  $(0.20nFAC_{\text{O}_2}D_{\text{O}_2}^{2/3}\nu^{-1/6})^{-1} = (Bn)^{-1}$ ). Given the essentially identical slope between all perovskite compositions and the platinum electrode (included as a reference in both Figures) under the same experimental conditions, the four-electron transfer pathway seems to be dominant in the ORR catalyzed using all perovskite oxides.<sup>8,10</sup> Further on, the term  $i_k^{-1} + i_f^{-1}$  can be obtained from the intercept of the plots, for example, at  $\omega^{-1/2} = 0$ . If, for the sake of argument,  $i_f$  is considered to be sufficiently large so that the intercept is equal to  $i_k^{-1}$ , then a lower intercept value suggests a higher ORR kinetic

current. As expected, platinum still provides the greatest performance; however, among the perovskite oxides considered here, the  $\text{LaCoO}_3$  and  $\text{LaNi}_{0.5}\text{Mn}_{0.5}\text{O}_3$  demonstrate the best performance in Figure 5a,b, respectively. It should be noted that these materials are far from optimized with respect to the carbon to perovskite loading and possibly with respect to available surface area, so the fact that the performance of some of the materials is close to Pt is very promising for further developments.

Insight into the ORR mechanism at the perovskite-modified RRDE could be obtained by analyzing the ring currents (Figure 6a,b), obtained simultaneously with the disk currents depicted in Figure 4a,b. The RRDE experiment involves holding the disk at a potential  $E_D$ , where the reaction  $O + ne \rightarrow R$  produces a cathodic current  $i_D$ ; the ring is kept at a sufficiently positive potential,  $E_R$ , that any  $R$  reaching the ring is rapidly oxidized, so that the concentration of  $R$  at the ring surface is essentially zero.<sup>23</sup> The ring current,  $i_R$ , is related to the disk current,  $i_D$ , by a quantity  $N$ , the collection efficiency; for example, the percentage of the hydroperoxide ion  $\text{HO}_2^-$  formed (eq 2) on the disk, which is detected on the ring,<sup>5,23</sup> as follows

$$N = \frac{-i_R}{i_D} \quad (7)$$

Moreover, the disk current,  $i_D$ , is the sum of the  $\text{O}_2$  reduction currents to water (four-electron pathway),  $i_{\text{H}_2\text{O}}$  and  $\text{O}_2$  reduction currents to hydroperoxide ion (two-electron pathway),  $i_{\text{HO}_2^-}$ ,<sup>12</sup> as follows

$$i_D = i_{\text{H}_2\text{O}} + i_{\text{HO}_2^-} \quad (8)$$

$$i_{\text{HO}_2^-} = \frac{i_R}{N} \quad (9)$$

The fraction of  $\text{HO}_2^-$  formation,  $x_{\text{HO}_2^-}$  can then be calculated from the molar flux rates of  $\text{O}_2$ ,  $n_{\text{O}_2(4e^-)}$ , and  $\text{HO}_2^-$ ,  $n_{\text{O}_2(2e^-)}$ ,<sup>12</sup> as follows

$$n_{\text{O}_2(4e^-)} = \frac{i_{\text{H}_2\text{O}}}{4F} \quad (10)$$

$$n_{\text{O}_2(2e^-)} = \frac{i_{\text{HO}_2^-}}{2F} \quad (11)$$

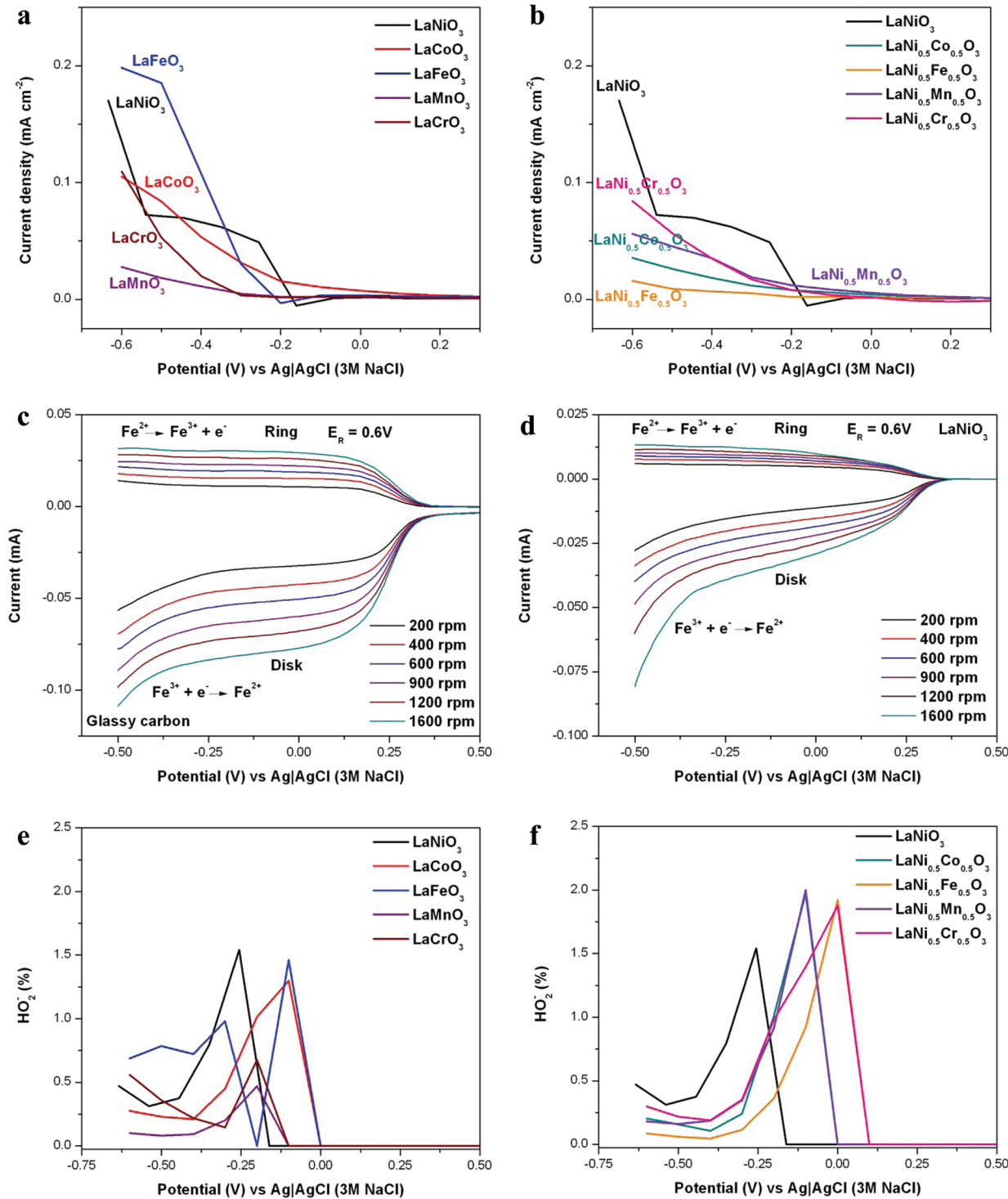


**Figure 6.** Ring current densities recorded on Pt ring electrode during ORR (simultaneously recorded with data in Figure 4a,b) using thin film of (a) LaNi<sub>3</sub>, LaCo<sub>3</sub>, LaFe<sub>3</sub>, LaMn<sub>3</sub>, and LaCr<sub>3</sub> and (b) LaNi<sub>0.5</sub>Co<sub>0.5</sub>O<sub>3</sub>, LaNi<sub>0.5</sub>Fe<sub>0.5</sub>O<sub>3</sub>, LaNi<sub>0.5</sub>Mn<sub>0.5</sub>O<sub>3</sub>, and LaNi<sub>0.5</sub>Cr<sub>0.5</sub>O<sub>3</sub> (all in oxygen-saturated 0.1 M KOH electrolyte using negative scan direction at 20 mV s<sup>-1</sup> scan rate); Ring (Fe<sup>2+</sup> → Fe<sup>3+</sup> + e<sup>-</sup>) and disk (Fe<sup>3+</sup> + e<sup>-</sup> → Fe<sup>2+</sup>) currents at room temperature for the determination of the collection efficiency on (c) glassy carbon disk RRDE and (d) thin film RRDE of LaNi<sub>3</sub> (both (c) and (d) in 1 M potassium chloride (KCl) supporting electrolyte with 1 mM K<sub>3</sub>Fe(CN)<sub>6</sub>); Percentage of hydrogen peroxide (H<sub>2</sub>O<sub>2</sub>) formation during ORR using thin film of (e) LaNi<sub>3</sub>, LaCo<sub>3</sub>, LaFe<sub>3</sub>, LaMn<sub>3</sub>, and LaCr<sub>3</sub> and (f) LaNi<sub>0.5</sub>Co<sub>0.5</sub>O<sub>3</sub>, LaNi<sub>0.5</sub>Fe<sub>0.5</sub>O<sub>3</sub>, LaNi<sub>0.5</sub>Mn<sub>0.5</sub>O<sub>3</sub>, and LaNi<sub>0.5</sub>Cr<sub>0.5</sub>O<sub>3</sub>.

$$x_{\text{H}_2\text{O}_2} = \frac{n_{\text{O}_2}(2\text{e}^-)}{n_{\text{O}_2}(2\text{e}^-) + n_{\text{O}_2}(4\text{e}^-)} = \frac{2i_{\text{R}}/N}{i_{\text{D}} + i_{\text{R}}/N} \quad (12)$$

For the collection experiments, two different disk electrodes were used to check the possibility of variation. The electrolyte

was a N<sub>2</sub>-saturated 1 M KCl (Sigma-Aldrich) with 1 mmol L<sup>-1</sup> K<sub>3</sub>Fe(CN)<sub>6</sub> (Merck p.a.). Figure 6c,d shows the voltammograms obtained for a bare and LaNi<sub>3</sub>-modified disk-RRDE, respectively. The voltammogram on the disk was obtained by potential scanning from 0.50 to -0.50 V versus Ag/AgCl

(3 M NaCl). Meanwhile, the ring potential was set at a constant 0.6 V; the potential at which the oxidation of  $[Fe(CN)_6]^{4-}$  back to  $[Fe(CN)_6]^{3-}$  occurs. Within the potential range examined and at rotation rates up to 1600 rpm, the collection efficiency are  $0.35 \pm 0.01$  and  $0.34 \pm 0.01$  for bare and LaNiO<sub>3</sub>-modified glassy carbon disk electrode, respectively which means that  $\sim 35$  and  $\sim 34\%$  of the product formed on the disk reaches the ring in the respective RRDE. The small differences between the former and the latter are probably due to the shape of the thin film layer, which tends to induce extra turbulence and thus slightly disturb  $[Fe(CN)_6]^{4-}$  collection in the ring. The latter value ( $0.34 \pm 0.01$ ) is used to calculate HO<sub>2</sub><sup>-</sup> formation (eq 2) according to eq 12 between 0.5 and  $-0.6$  V, the results of which are shown in Figure 6e,f. Figure 6e displays that the maximum HO<sub>2</sub><sup>-</sup> formation is only  $\sim 1.5\%$ , with the maximum formation centered at potential range between approximately  $-0.05$  and  $-0.3$  V. As a general trend, among LaNiO<sub>3</sub>, LaCoO<sub>3</sub>, LaFeO<sub>3</sub>, LaMnO<sub>3</sub>, and LaCrO<sub>3</sub>, HO<sub>2</sub><sup>-</sup> amount lessens in the order of LaNiO<sub>3</sub>, LaFeO<sub>3</sub>, LaCoO<sub>3</sub>, LaCrO<sub>3</sub>, and LaMnO<sub>3</sub>. Figure 6f evidences slightly larger formation of HO<sub>2</sub><sup>-</sup> for LaNi<sub>0.5</sub>Mn<sub>0.5</sub>O<sub>3</sub>, LaNi<sub>0.5</sub>Cr<sub>0.5</sub>O<sub>3</sub>, LaNi<sub>0.5</sub>Co<sub>0.5</sub>O<sub>3</sub>, and LaNi<sub>0.5</sub>Fe<sub>0.5</sub>O<sub>3</sub> (LaNiO<sub>3</sub> as a reference), reaching a maximum percentage of  $\sim 2.0\%$ . While the HO<sub>2</sub><sup>-</sup> formation trends for these compositions (Figure 6f) are quite similar to each other, the maximum HO<sub>2</sub><sup>-</sup> formation seems to shift to a more positive potentials range, for example,  $\sim 0.1$  to  $-0.25$  V; consistent with the shift of ORR onset to more positive potential for LaNi<sub>0.5</sub>M<sub>0.5</sub>O<sub>3</sub>. Overall, the results presented in Figure 6e,f are also in good agreement with the previous results in Figure 5a,b regarding the domination of four-electron pathway in the ORR using synthesized perovskite oxides.

## CONCLUSIONS

The intrinsic catalytic activity of La-based perovskite oxides was studied by thin-film RRDE. Among the LaMO<sub>3</sub> (M = Ni, Co, Fe, Mn, and Cr)-modified disk RRDE, LaCoO<sub>3</sub> shows the largest ORR current density and most positive onset potential, offering a clear direction for further study of transition-metal cation substitution. Similarly, between LaNi<sub>0.5</sub>M<sub>0.5</sub>O<sub>3</sub> (M = Ni, Co, Fe, Mn, and Cr)-modified disk electrodes, LaNi<sub>0.5</sub>Mn<sub>0.5</sub>O<sub>3</sub> displays the largest current density and most positive onset potential. Catalytic enhancement is clearly noted upon, substituting half of Ni in LaNiO<sub>3</sub> with other metal cations. Koutecky-Levich plots for all oxide compositions provide similar slope with respect to platinum, implying that the ORR proceeds in four-electron transfer pathway. This observation is further supported by detection of  $<2\%$  of the hydroperoxide ion formed during the negative scan from 0.5 to  $-0.75$  V.

## AUTHOR INFORMATION

### Corresponding Author

\*E-mail: j.sunarso@deakin.edu.au; maria.forsyth@deakin.edu.au.

### Notes

The authors declare no competing financial interest.

## ACKNOWLEDGMENTS

J.S. acknowledges Alfred Deakin Postdoctoral Research Fellowship (RM23088) from Deakin University which enables this project. The authors also gratefully acknowledge the financial support from the Australian Research Council (ARC) through the ARC Centre of Excellence for Electromaterials Science

## REFERENCES

- Neburchilov, V.; Wang, H.; Martin, J. J.; Qu, W. *J. Power Sources* **2010**, *195*, 1271.
- Gasteiger, H. A.; Kocha, S. S.; Sompalli, B.; Wagner, F. T. *Appl. Catal., B* **2005**, *56*, 9.
- Jörissen, L. *J. Power Sources* **2006**, *155*, 23.
- Choi, J.-Y.; Hsu, R. S.; Chen, Z. *J. Phys. Chem. C* **2010**, *114*, 8048.
- Roche, I.; Chaînet, E.; Chatenet, M.; Vondrák, J. *J. Phys. Chem. C* **2007**, *111*, 1434.
- Shao, M.-H.; Sasaki, K.; Adzic, R. R. *J. Am. Chem. Soc.* **2006**, *128*, 3526.
- Suntivich, J.; Gasteiger, H. A.; Yabuuchi, N.; Nakanishi, H.; Goodenough, J. B.; Shao-Horn, Y. *Nat. Chem.* **2011**, *3*, 546.
- Suntivich, J.; Gasteiger, H. A.; Yabuuchi, N.; Shao-Horn, Y. *J. Electrochem. Soc.* **2010**, *157*, B1263.
- Wang, H.; Liang, Y.; Li, Y.; Dai, H. *Angew. Chem., Int. Ed.* **2011**, *50*, 1.
- Winther-Jensen, B.; Winther-Jensen, O.; Forsyth, M.; MacFarlane, D. R. *Science* **2008**, *321*.
- Xu, J.; Gao, P.; Zhao, T. S. *Energy Environ. Sci.* **2012**, *5*, 5333.
- Paulus, U. A.; Schmidt, T. J.; Gasteiger, H. A.; Behm, R. J. *J. Electroanal. Chem.* **2001**, *495*, 134.
- Gasteiger, H. A.; Garche, J. *Fuel Cells*; Wiley-VCH: Weinheim, Germany, 2008.
- Li, X.; Li Zhu, A.; Qu, W.; Wang, H.; Hui, R.; Zhang, L.; Zhang, J. *Electrochim. Acta* **2010**, *55*, 5891.
- Li, X.; Qu, W.; Zhang, J.; Wang, H. *J. Electrochem. Soc.* **2011**, *158*, A597.
- Niu, Y.; Sunarso, J.; Liang, F.; Zhou, W.; Zhu, Z.; Shao, Z. *J. Electrochim. Soc.* **2011**, *158*, B132.
- Hyodo, T.; Hayashi, M.; Miura, N.; Yamazoe, N. *J. Electrochim. Soc.* **1996**, *143*, L266.
- Coelho, A. *DIFFRACplus TOPAS 4.2*; BrukerAXS: Karlsruhe, Germany, 2008.
- Joint Committee on Powder Diffraction Standards (JCPDS)-International Centre for Diffraction Data (ICDD): Pennsylvania, 2010.
- TIMCAL Ltd., CH-Bodio, 2005. [http://www.timcal.com/scopi/group/timcal/timcal.nsf/pagesref/MCOA-7S6K2K/\\$File/Brochure\\_Carbon\\_Powders\\_for\\_Lithium\\_Battery\\_Systems.pdf](http://www.timcal.com/scopi/group/timcal/timcal.nsf/pagesref/MCOA-7S6K2K/$File/Brochure_Carbon_Powders_for_Lithium_Battery_Systems.pdf) (accessed February 9, 2011).
- Schmidt, T. J.; Gasteiger, H. A.; Stäb, G. D.; Urban, P. M.; Kolb, D. M.; Behm, R. J. *J. Electrochim. Soc.* **1998**, *145*, 2354.
- Stamenković, V.; Schmidt, T. J.; Ross, P. N.; Marković, N. M. *J. Phys. Chem. B* **2002**, *106*, 11970.
- Bard, A. J.; Faulkner, L. R. *Electrochemical Methods: Fundamental and Applications*, 2nd ed.; John Wiley & Sons, Inc.: Hoboken, NJ, 2001.